Supporting Information

A hydrogel gripper enabling fine movement based on spatiotemporal mineralization

Liangrui Zuo[a], Mingzhen Wu[b], Hongbo Zhang[a], Shikai Zhang[a], Zhengxin Ma[a], Jun Luo[a],

Chunmei Ding[a]*, Jianshu Li[a,c,d]*

[a] College of Polymer Science and Engineering, State Key Laboratory of Polymer Materials Engineering, Sichuan University, Chengdu 610065, China

[b] Guangxi Institute for Food and Drug Control, Nanning 530021, China

[c] State Key Laboratory of Oral Diseases, West China Hospital of Stomatology, Sichuan University, Chengdu 610041, China

[d] Med-X Center for Materials, Sichuan University 610041, China

*Corresponding Authors.

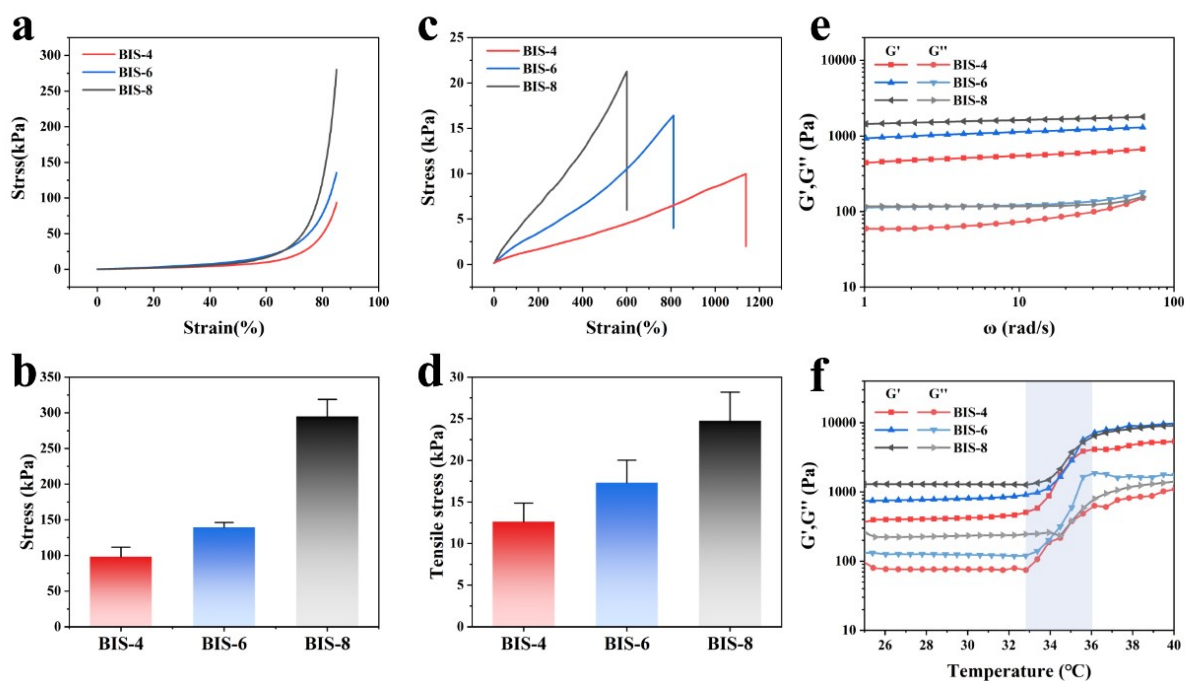E-mail addresses: jianshu_li@scu.edu.cn (J.S. Li); E-mail addresses: dingcm@scu.edu.cn(C.M. Ding)

Figure S1 Mechanical and rheological properties of PNIPAM hydrogels with different BIS contents. (a) Compression curves of hydrogels. (b) Compressive strength of hydrogels at the strain of 85%. (c) Tensile curves of PH with different BIS contents. (d) Tensile strength of hydrogels. (e) Storage and loss moduli of hydrogels as a function of frequency (ω). (f) Storage and loss moduli of hydrogels as a function of temperature.

The concentration of crosslinker (BIS in this work) was tuned to estimate the mechanical properties of hydrogel, considering the degree of crosslinking plays a dominated role.[1] Specifically, compression, tensile, and rheological tests were performed to screen for BIS

contents in PH with the best mechanical properties (Figure S1). It can be seen that the mechanical properties of the gel improved with the increase of BIS content (Figure 2a-d). When the compressive strain was set to 85%, the stress of the hydrogel in the BIS-4 group was 98.2 kPa, while that for BIS-6 and BIS-8 groups was 139.6 kPa and 294.8 kPa respectively (Figure S1a and b). Similar trend was observed for the tensile tests (Figure S1c and d): the higher the content of BIS, the higher the breaking strength and the smaller the elongation at break. The breaking strengths of BIS-4, BIS-6 and BIS-8 were 12.6 kPa, 17.3 kPa and 24.8 kPa respectively, and the elongation at break was 1139%, 810% and 600% correspondingly. Based on above, a higher content of BIS results in a greater crosslinking density and a stiffer hydrogel. Therefore, BIS-8 hydrogels have the highest mechanical strength among the three, in good accordance with the previous literatures.[2] It should be mentioned that a content of crosslinker higher than 8 mg leads to the relative low tolerance of hydrogel to tensile stress, so the maximum BIS of 8 mg was adopted in this experiment.

Figure S1e represents the rheological curves of PH with different BIS contents under frequency scanning. The storage modulus (G') of PH is greater than the loss modulus (G''), which reveals the gel-behavior under the test conditions. The linear viscoelastic region of G' denotes the stable mechanical performance of the hydrogels, which increased with the increment of BIS cross-linker (400 Pa, 867 Pa and 1407 Pa for BIS-4, BIS-6 and BIS-8 respectively). This reflects that a higher BIS content results in a higher storage modulus of PH. This law is consistent with the previous mechanical test results.

Apart from the mechanical properties, the thermosensitive behavior of PNIPAM hydrogel is of guiding significance for the subsequent photothermal actuation. The rheology of hydrogels was thus tested as a function of temperature (25-40 °C). When the temperature raised from 25 °C to

32 °C, the G' and G" of hydrogel remained stable. By contrast, the temperature region of 32 °C to 36 °C drives the drastic increase of G' and G", which then slightly changed under a further increment of temperature (Figure S1f). It should be mentioned that PNIPAM conducted abrupt modulus changes at the temperature range of 32 °C to 36 °C. Under these circumstances, the hydrophilic interaction between water and the isopropylamide groups was weakened, accompanied with the intense hydrophobic interactions among the hydrophobic moieties (methyl/ methylene groups).[3] The molecular chain network of PNIPAM shrunk with the release of water, so the G' increased. In combination with that, phase separation of PNIPAM occurred, which accounted for the improvement of the viscosity and loss modulus.

Note that the phase transition temperature of all hydrogels (BIS-4, BIS-6 and BIS-8) located in the range of 32-36 °C, and there were no significant differences among diverse hydrogel. Compared with BIS-4 and BIS-6 hydrogels, BIS-8 hydrogel had the best mechanical property and highest storage modulus. This prominent property enabled the powerful grasp of objects by hydrogel actuators, we thus chose BIS-8 hydrogel in subsequent experiments.
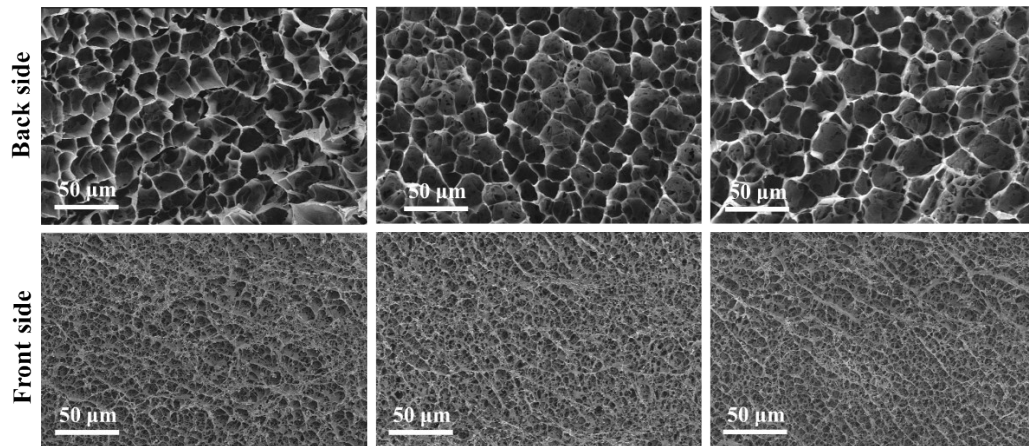
Figure S2. The SEM images of the front side and the back side of 3 parallel PNIPAM hydrogels with UV irradiation for 12min.
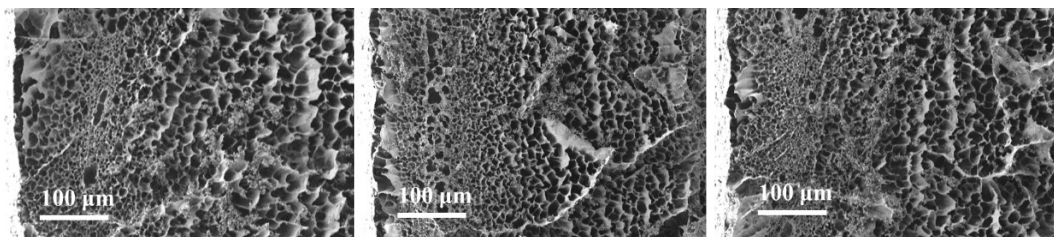

Figure S3. The SEM images of the cross section of 3 parallel PNIPAM hydrogels
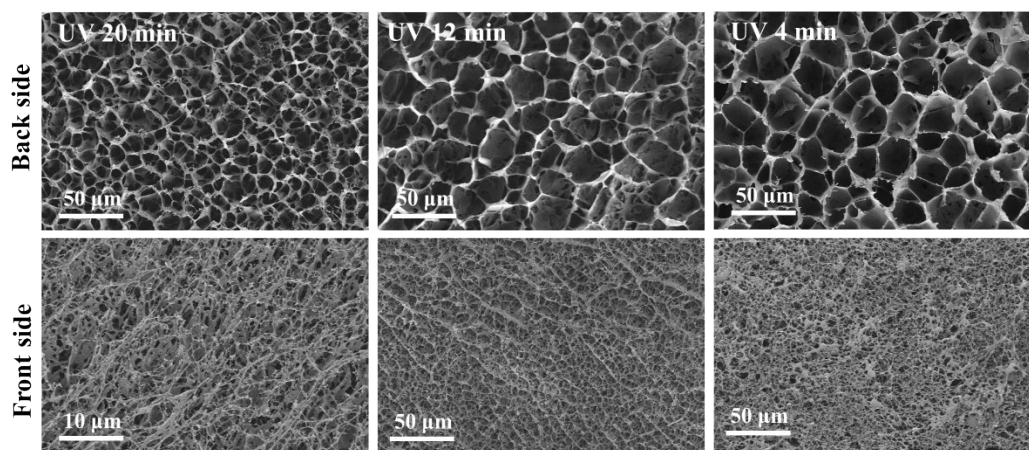

Figure S4. The SEM images of the front side and the back side of PNIPAM hydrogels with UV irradiation for 20, 12 and 4 min, respectively.
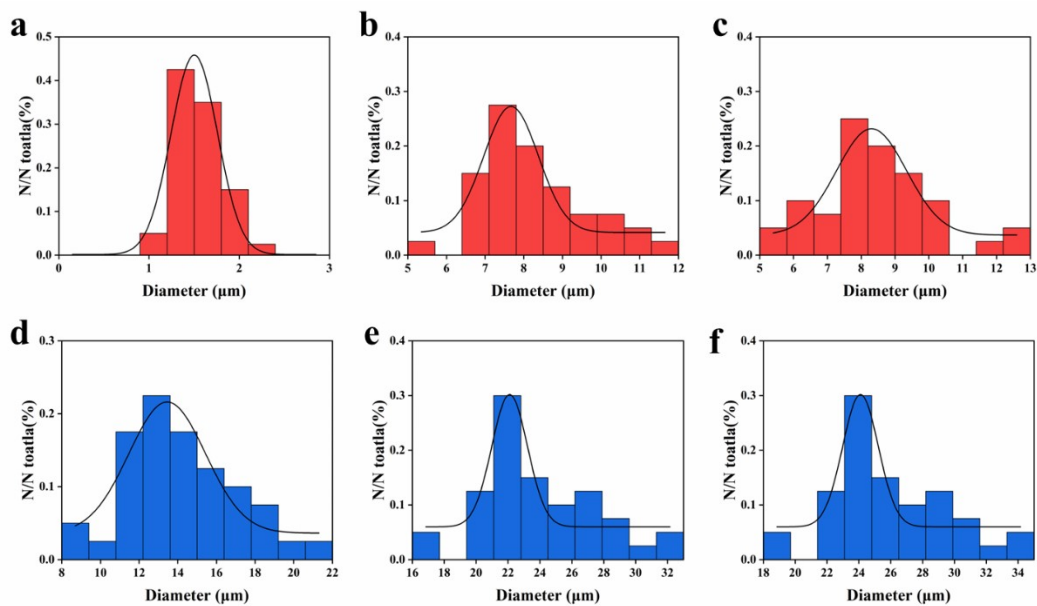
Figure S5. Pore diameter distribution of the back side of PNIPAM hydrogel with UV irradiation for 20 min (a), 12 min (b) and 4 min (c), respectively. Pore diameter distribution of the front side of PNIPAM hydrogel with UV irradiation for 20 min (d), 12 min (e) and 4 min (f), respectively.
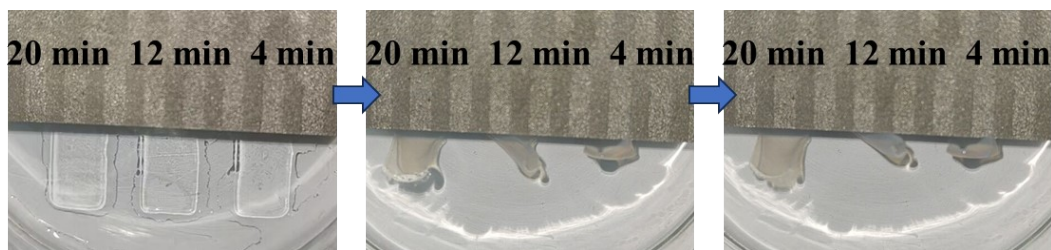

Figure S6. Images of deformation of PNIPAM hydrogel with different times of UV irradiation in hot water.

$$\cos\theta_r = f1\cos\theta_1 + f2\cos\theta_2 \qquad \textbf{Equation S1}$$

Among them, θ_1 and θ_2 is the intrinsic contact angle of the surface of component 1 and component 2. f1 and f2 stands for the apparent area fraction of component 1 and component 2 ($f_1 + f_2 = 1$). Here, component 1 represents polymer matrix, and component 2 represents water. Therefore, $\theta_2 = 0\,°$, $\cos\theta_2 = 1$. When the pore size of the hydrogel surface is smaller, the f2 will be larger, which results in the lager $\cos\theta_r$ and smaller θ_r.
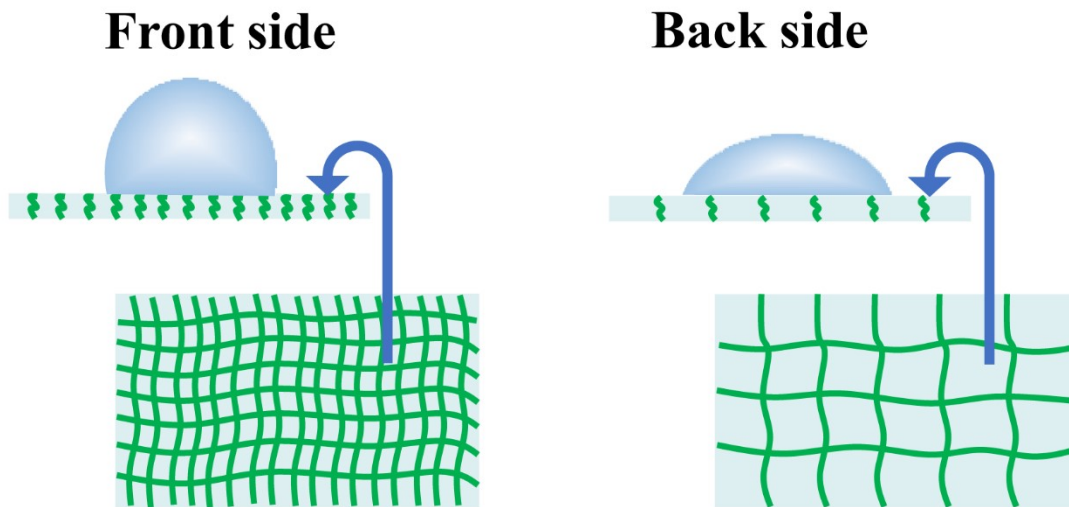

Figure S7. Schematic diagram of water droplets on the front and back side of hydrogel.
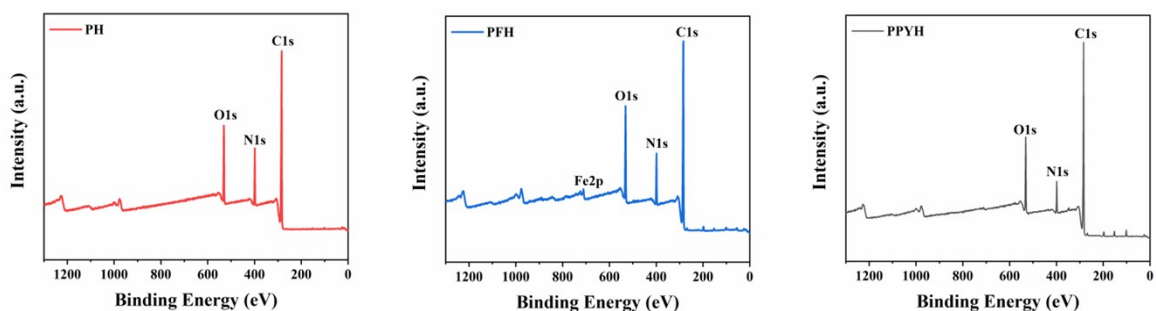
Figure S8. The full XPS spectrum of PH, PFH, PPYH.

XPS spectra were further measured to clarify the detailed constitutions of hydrogels. The full XPS spectra indicate intense peaks of C1s, N1s and O1s in all groups (Figure S3). In addition, obvious peaks of Fe2p were especially detected in PFH. The high-resolution spectra were used to further analyze the surface chemical structure of PH, PFH and PPYH. The C 1s high-resolution spectra of PH suggested obvious C-C (285 eV), C-N (286 eV) and C=O (287 eV) states, assignable to the main chain and amide moieties in PNIPAM (Figure S4a).[4] The characteristic peaks of Fe 2p 1/2 (725 eV) and Fe 2p 3/2 (711 eV) in the Fe 2p high-resolution spectra of PFH were attributed to the $Fe(OH)_3$ minerals after mineralization (Figure S4b).[5] The existence of $Fe(OH)_3$ was also confirmed by the Fe-OH peak at 530.6 eV and Fe-O peak at 531.3 eV in the O 1s high-resolution spectrum of PFH (Figure S4c).[6] Besides, weak peaks of Fe 2p 1/2 and Fe 2p 3/2 were also observed in the Fe 2p high-resolution spectra of PPYH, while the O 1s high-resolution spectra of PPYH resembled that of PFH. These results again proved that slight Fe was not completely removed by post-treatment during the experiment. The peaks at 398.8 eV, 399.3 eV and 400.2 eV in the N 1s high-resolution spectra of PPYH are corresponding to =NH-, -NH- and $-HN^+-$ states, which are attributed to the newly generated pyrrole groups in PPYH (Figure S4d).[7]
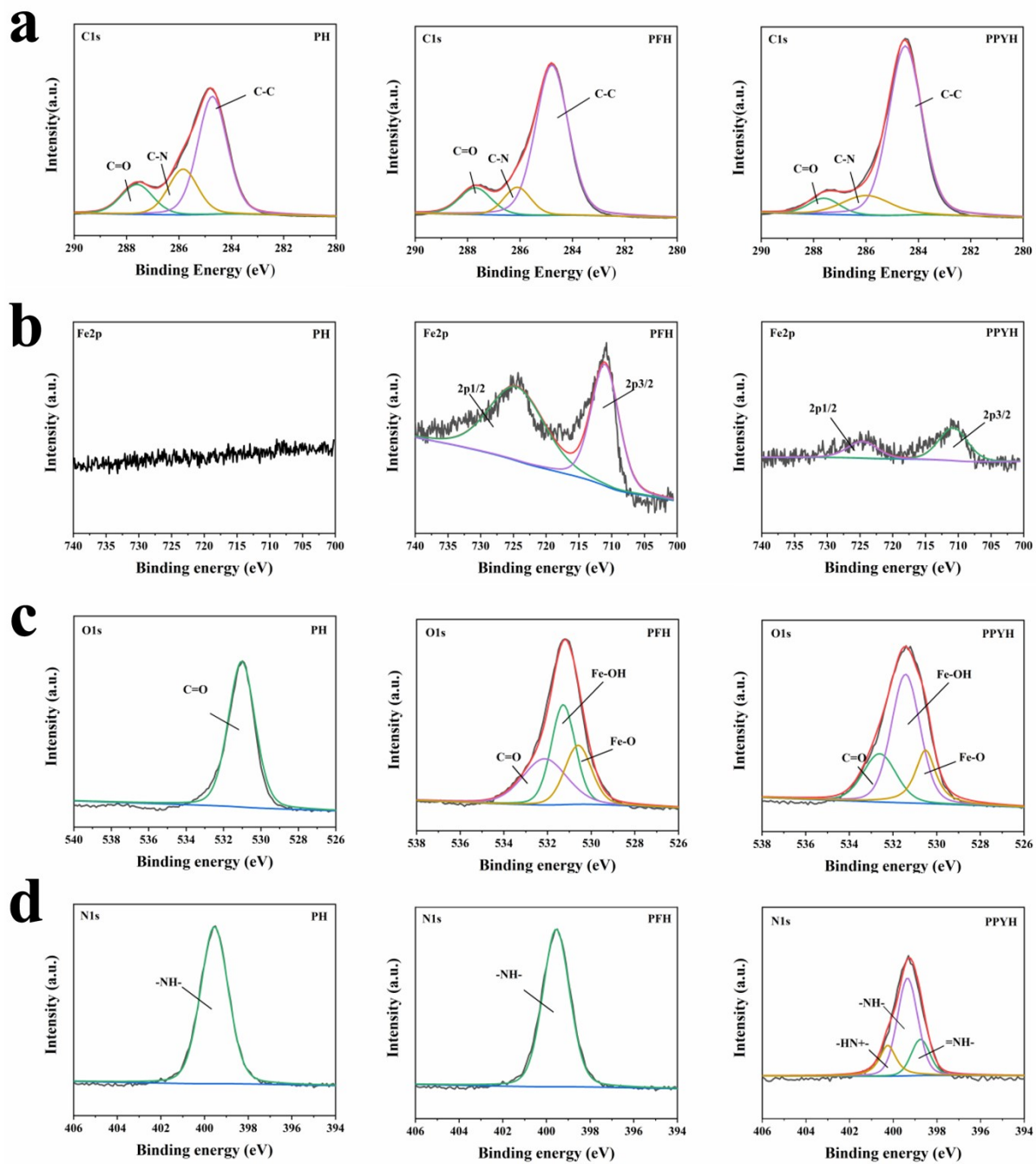
Figure S9. (a) The C 1s, (b) Fe 2p, (c) O 1s, (d) N 1s high-resolution spectra of PH, PFH and PPYH.
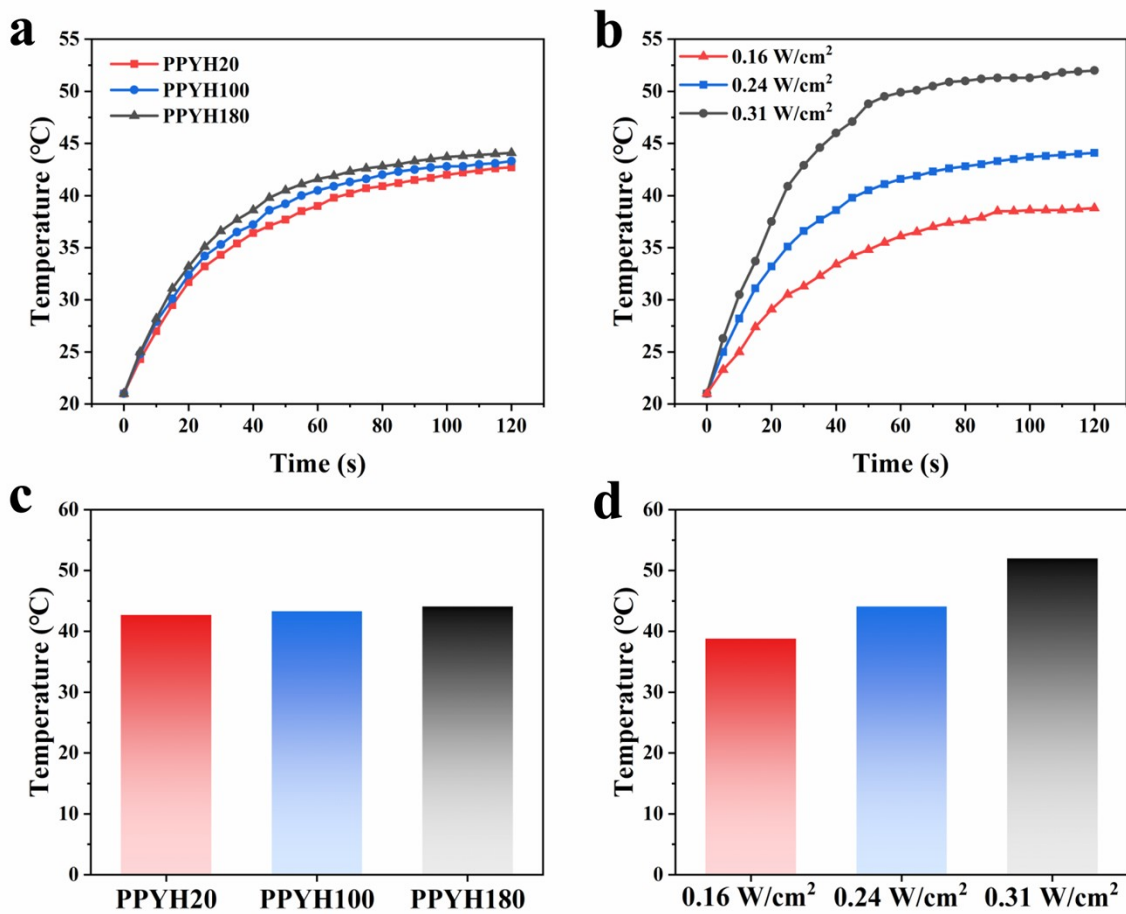
Figure S10. (a) Time-dependent temperature change curves of PPYH20, PPYH100 and PPYH180 under NIR light irradiations (808nm, 0.24 W/cm^2) (b) Time-dependent temperature change curves of PPYH180 under NIR light irradiations with different power densities. (c) Statistics temperature changes of PPYH20, PPYH100 and PPYH180 under NIR irradiation for 2 minutes (808 nm, 0.24 W/cm^2). (d) Statistical temperature changes of PPYH180 under NIR irradiation for 2 minutes with different powers.
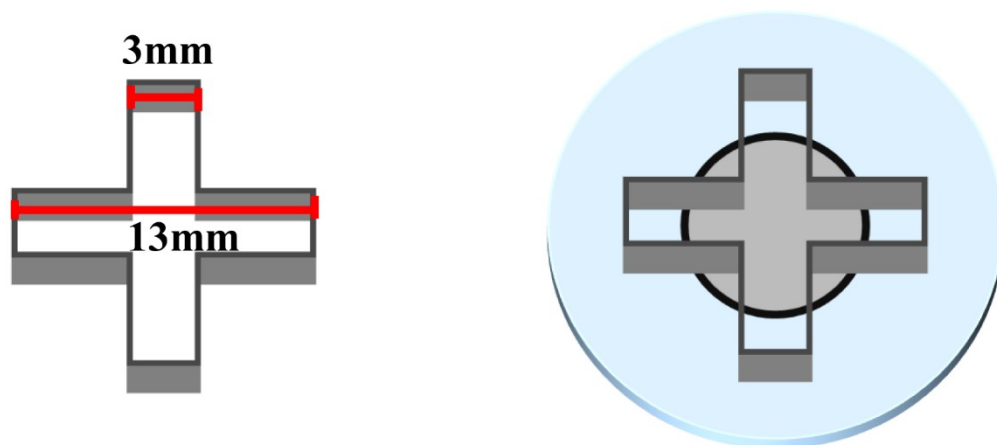
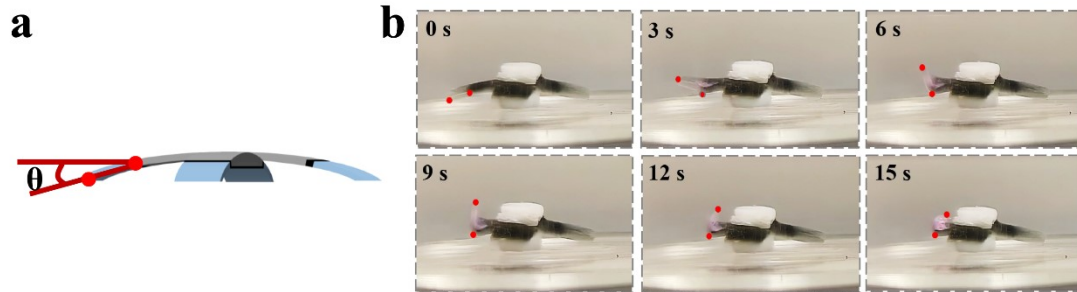**Figure S11.** Schematic diagram for the preparation of gripper by cutting PPYH with a cruciform mold.

Figure S12. (a) Illustration of bending angle of PPYH. (b) Deformation process of the PPYH180 actuator under NIR light irradiation.
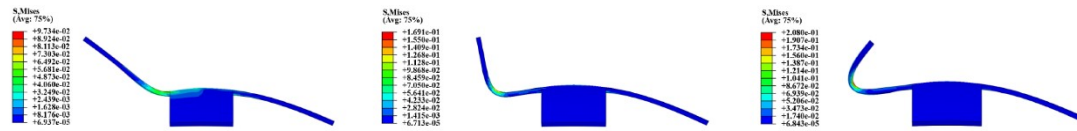
Figure S13. The finite element simulation results of driving deformation of PPYH20, PPYH100 and PPYH180 under NIR light.

Figure S14. (a)Typical time-dependent temperature change curves of PPYH after 0 ultrasound, 1 ultrasound and 2 ultrasounds under NIR light irradiations (808nm, 0.24 W/cm^2). Each ultrasound lasted for 3 minutes. (b) The corresponding statistics temperature of PPYH after 120 s.

Figure S15. Raman spectrum of PPYH after 2 ultrasounds. Each ultrasound lasted for 3 minutes.

Table S1. Elemental content of PH, PFH and PPYH.

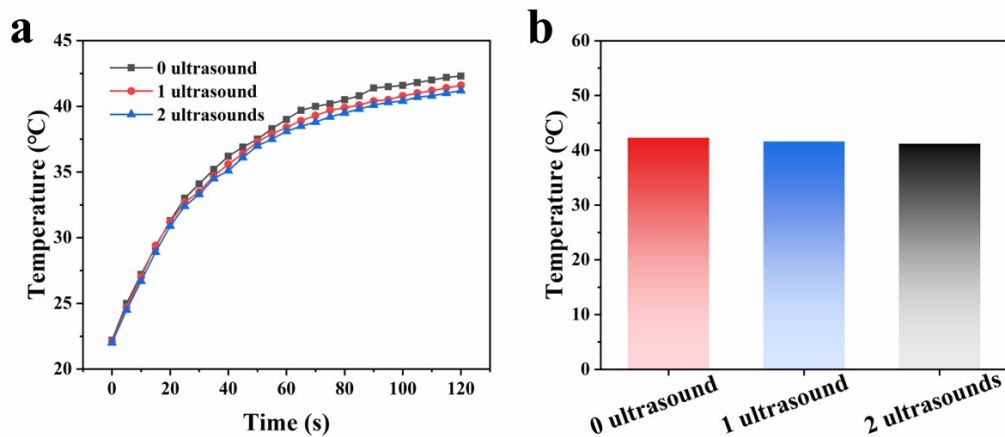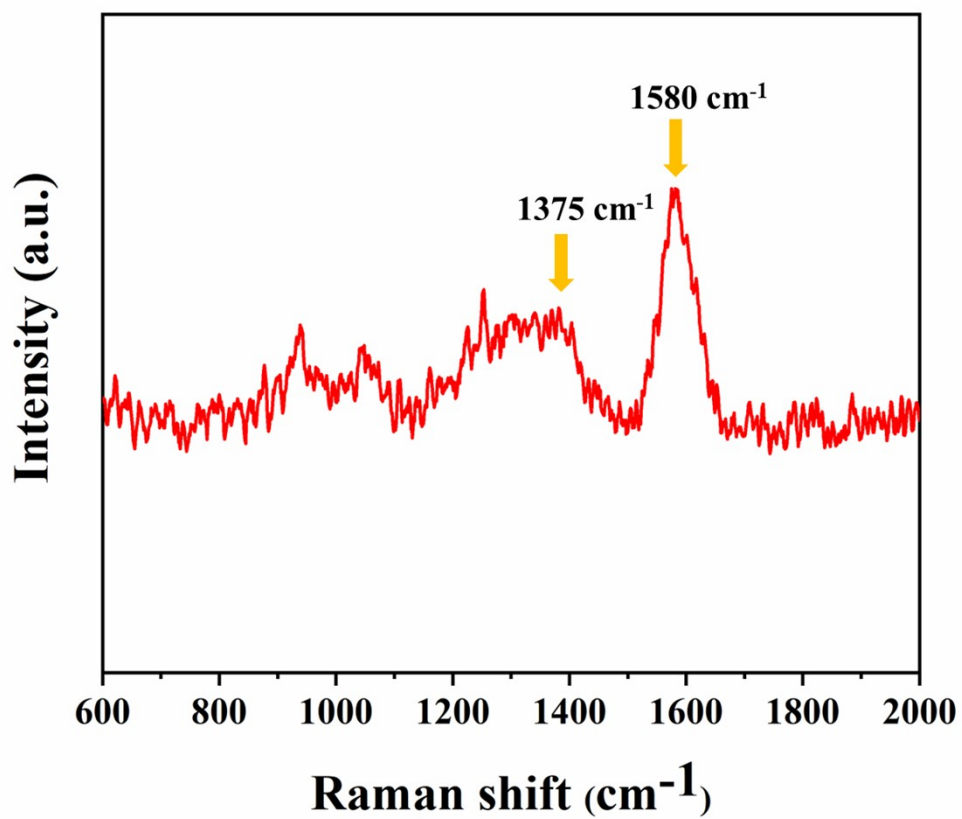| Element	Atomic percentage of PH (%)	Atomic percentage of PFH (%)	Atomic percentage of PPYH (%)
C	75.07	65.86	69.49
N	12.38	10.83	11.51
O	12.55	19.23	18.63
Fe	0	4.09	0.36

Table S2. The component, actuating type, mechanical properties and preparation methods of hydrogel actuator.

Components	Actuating types	Mechanical properties	Preparation methods	References
AAm, BIS, Eu·L3, Tb • L3, NIPAM, chitosan, DEAP	pH, temperature	tensile fracture strength: 5-55 kPa tensile fracture elongation: 280%-640%	Photopolymerization (mercury lamp), two-step synthesis	[8]
HETAC, HEAA, VBIPS, BIS, 2-hydroxy-4′-(2-hydroxyethoxy)-2-methylpropiophenone	Salt	tensile fracture strength: 21 to 104 kPa tensile fracture elongation: 145%-978%	Photopolymerization (UV light), two-step synthesis	[9]
AMPS, AAm, rGO, KPS	Electric	tensile fracture strength: 24 to 97 kPa tensile fracture elongation: 130%-297%	Thermal-initiated polymerization	[10]
DMAPMA, NIPAM, MMT, BIS, TEMED, KPS	pH, temperature	tensile fracture strength: 41-51 kPa tensile fracture elongation: 142%-277%	Thermal-initiated polymerization, two-step synthesis	[11]
NIPAM, BIS, APS, TEMED, BN, AlN, Si3N4,	Temperature	tensile fracture strength: 12-18 kPa tensile fracture	Photopolymerization (UV light)	[12]

		elongation: 50%-200%		
NIPAM, BIS, KPS, TEMED, Ag nanoparticles	**Temperature**	**tensile fracture strength: 25.2 kPa** **tensile fracture elongation: 535%**	**Thermal-initiated polymerization**	13
NIPAM, KPS, TEMED, Au/g-C3N4 nanoparticles	**Temperature，NIR light**	**tensile fracture strength: 13-94 kPa** **tensile fracture elongation: 16%-232%**	**Thermal-initiated polymerization**	14
NIPAM, MBAA, I2959, pyrrole	**Temperature, NIR light**	**tensile fracture strength: 24.8 kPa** **tensile fracture elongation: 600%**	**Photopolymerization (UV light)**	**This work**

AAm: Acrylamide; AMPS :2-acrylamido-2-methylpropanesulfonic acid; L3: Eu/2,6-pyridinedicarboxylic acid complexes with polymerizable sites; Eu·L3: Eu/L3; Tb·L3: Tb/L3; DEAP: 2,2-diethoxyacetophenone; GO: Graphene oxide; AMPS: 2-Acrylamido-2-methylpropanesulfonic acid; METAC: [2-methacryloyloxy)ethyl]trimethylammonium chloride; VBIPS: 3-(1-(4-vinylbenzyl)-1H-imidazol-3-ium-3-yl)propane-1-sulfonate; HEAA: N-(2-Hydroxyethyl)acrylamide; KPS: Potassium persulfate; 2-hydroxy-4′-(2-hydroxyethoxy)-2-methylpropiophenone；TEMED: N,N,N′,N′-tetramethylethylenediamine；DMAPMA: N-[3-(dimethylamino)propyl] methacrylamide; MMT: Montmorillonite; APS: Ammonium persulfate;

REFERENCES

1.   A. A. M. Shimojo, A. M. B. Pires, R. Lichy, A. A. Rodrigues and M. H. A. Santana, *J. Biomed. Mater. Res. Part A*, 2015, **103**, 730-737.
2.   J. Su, Y. Yang, Z. Chen, J. Zhou, X. Liu, Y. Fang and Y. Cui, *Polym. Int.*, 2019, **68**, 1673-1680.
3.   X.-Z. Zhang, X.-D. Xu, S.-X. Cheng and R.-X. Zhuo, *Soft Matter*, 2008, **4**, 385-391.
4.   H. Zheng, S. Zhang, C. Yang, H. Yin, W. Liu and K. Lu, *J. Mol. Liq.*, 2021, **342**.
5.   G. Bhargava, I. Gouzman, C. M. Chun, T. A. Ramanarayanan and S. L. Bernasek, *Appl.*

Surf. Sci., 2007, **253**, 4322-4329.

6. G. Cui, M. Liu, Y. Chen, W. Zhang and J. Zhao, *Carbohydr Polym*, 2016, **154**, 40-47.
7. A. E. Jaouhari, S. B. Jadi, A. E. Guerraf, M. Bouabdallaoui, Z. Aouzal, E. A. Bazzaoui, J. I. Martins and M. Bazzaoui, *Synth. Met.*, 2018, **245**, 237-244.
8. B. Li, Z. Song, K. Zhu, Q. Niu, Z. Li and H. Li, *ACS Appl. Mater. Interfaces*, 2021, **13**, 20633-20640.
9. S. Xiao, Y. Yang, M. Zhong, H. Chen, Y. Zhang, J. Yang and J. Zheng, *ACS Appl. Mater. Interfaces*, 2017, **9**, 20843-20851.
10. C. Yang, Z. Liu, C. Chen, K. Shi, L. Zhang, X. J. Ju, W. Wang, R. Xie and L. Y. Chu, *ACS Appl. Mater. Interfaces*, 2017, **9**, 15758-15767.
11. G. Gao, L. Wang, Y. Cong, Z. Wang, Y. Zhou, R. Wang, J. Chen and J. Fu, *ACS Omega*, 2018, **3**, 17914-17921.
12. Z. Chen, Y. Chen, C. Chen, X. Zheng, H. Li and H. Liu, *Chem. Eng. J.*, 2021, **424**.
13. H. Liu, X. Jia, R. Liu, K. Chen, Z. Wang, T. Lyu, X. Cui, Y. Zhao and Y. Tian, *J. Mater. Chem. A*, 2022, **10**, 21874-21883.
14. P. Chen, Q. Ruan, R. Nasseri, H. Zhang, X. Xi, H. Xia, G. Xu, Q. Xie, C. Yi, Z. Sun, H. Shahsavan and W. Zhang, *Adv. Sci.*, 2022, **9**, e2204730.